THE JOURNAL OF PHYSICAL CHEMISTRY LETTERS
A JOURNAL OF THE AMERICAN CHEMICAL SOCIETY

pubs.acs.org/JPCL Letter

Coupled Spin-Valley, Rashba Effect, and Hidden Spin Polarization in WSi_2N_4 Family

Sajjan Sheoran,* Sanchi Monga, Ankita Phutela, and Saswata Bhattacharya*

Cite This: *J. Phys. Chem. Lett.* 2023, 14, 1494−1503 Read Online

ACCESS | Metrics & More | Article Recommendations | Supporting Information

ABSTRACT: Using first-principles calculations, we report the electronic properties with a special focus on the band splitting in the WSi_2N_4 class of materials. Due to the broken inversion symmetry and strong spin−orbit coupling, we detect coupled spin-valley effects at the corners of the first Brillouin zone (BZ). Additionally, we observe cubically and linearly split bands around the Γ and M points, respectively. The in-plane mirror symmetry (σ_h) and reduced symmetry of the arbitrary ***k***-point, enforce the persistent spin textures (PST) to occur in full BZ. We induce the Rashba splitting by breaking the σ_h through an out-of-plane external electric field (EEF). The inversion asymmetric site point group of the W atom introduces the hidden spin polarization in centrosymmetric layered bulk counterparts. Low energy ***k.p*** models demonstrate that the PST along the M−K line is robust to EEF and layer thickness, making them suitable for applications in spintronics and valleytronics.

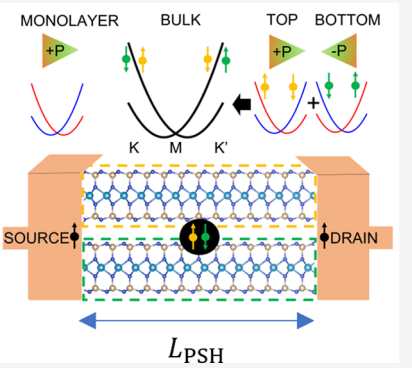

The discovery of graphene has enormously revolutionized the field of atomically thin two-dimensional (2D) materials because of its extraordinary electronic properties compared to the bulk counterparts.[1−5] Recent advancements in experimental techniques have explored many new 2D materials beyond graphene, including germanene,[6] silicene,[7] 2D boron nitride,[8,9] 2D transition metal dichalcogenides (TMDs),[10−14] and transition metal carbides/nitrides (MXenes).[15,16] The septuple atomic layer 2D materials $MoSi_2N_4$ and WSi_2N_4 have been experimentally synthesized by passivating the surfaces of nonlayered materials.[17] These materials have a semiconducting nature with excellent ambient stability, high strength, and considerable carrier mobility. After that, theoretical studies based on density functional theory (DFT) have predicted several similar thermodynamically stable compounds having formula MA_2Z_4 (M is an early transition metal, viz., Cr, Mo, W, V, Nb, Ta, Ti, Zr, or Hf; A = Si or Ge; Z = N, P, or As) .[18] Subsequent studies have revealed that these materials have promising electronic, optical, mechanical, thermal, and nontrivial topological properties.[19−25] Moreover, straining, twisting, and stacking of these 2D layers to form heterostructures and moire superlattices tune their electronic properties.[26−30]

The progress in 2D materials also generates the impetus for realizing physical properties desirable in spintronics and valleytronics. In condensed matter physics, discussion of the symmetry in crystalline solids plays a pivotal role in understanding the physical properties. For instance, inversion and time-reversal symmetry together force the bands to be doubly degenerate throughout the Brillouin Zone (BZ). The coupling of inversion symmetry breaking with spin−orbit coupling (SOC) lifts the band degeneracy mainly through Rashba and Dresselhaus effects. However, if time-reversal symmetry breaks along with inversion symmetry breaking, the spin-valley effects are induced. The presence of well-separated multiple energy extremal points in momentum-space, generally referred to as valleys, constitutes a binary index for low energy carriers.[31] Valley index is robust to the scattering by smooth deformations and long-wavelength phonons. Therefore, it can be exploited for information processing and encoding. The lifting of band degeneracy results in nontrivial momentum-dependent spin textures, which are mainly governed by the type of splitting. In general, the SOC introducing these spin splitting effects, also introduces two kinds of spin dephasing mechanisms, viz., Dyakonov-Perel[32] and Elliot-Yafet[33] mechanisms. One of the possible ways to overcome these spin dephasing mechanisms is persistent spin texture (PST), in which spin directions become independent of the crystal momentum (***k***).[34] PST is obtained by trading off the strength of the linear Rashba and Dresselhaus effects in heterostructures and surfaces. It has also been shown that nonsymmorphic space group symmetry could be exploited to obtain PST around specific high symmetry points and paths.[35] Also, cubic spin splittings can lead to symmetry-protected PST around the zone center in bulk materials.[36] Analogous to charge, utilizing

Received: October 12, 2022
Accepted: February 1, 2023
Published: February 6, 2023

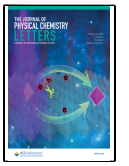

https://doi.org/10.1021/acs.jpclett.2c03108
J. Phys. Chem. Lett. 2023, 14, 1494−1503

the spin and valley degrees of freedom through the nondissipative spin transport is a vital ingredient of spintronics and valleytronics.

The 2D $MoSi_2N_4$, WSi_2N_4, and $MoSi_2As_4$ host massive Dirac Fermions with strong spin valley coupling near the corners of BZ. Additionally, the valley Fermions manifest valley-contrasting Berry curvature, and valley-selective optical circular dichroism.[20,37,38] This can be attributed to the intrinsic broken inversion symmetry coupled with large SOC arising from *d*-orbitals of transition metals. Under an in-plane electric field, carriers in different valleys drift in opposite directions, leading to the valley Hall effect. $MoSi_2N_4$ shows exceptional piezoelectricity, photocatalytic water splitting, and high carrier mobility of 270−1200 $cm^2/(V\ s)$, which is better than widely used TMDs.[22] The stacking of $MoSi_2N_4$ monolayers generates a dynamically stable bilayer and bulk materials with thickness-dependent properties.[39] Most of the studies focus on the valley splitting in monolayers around the corners of the BZ. However, the complete analysis of SOC induced spin splitting is still unclear.

This work reports fully relativistic calculations within the framework of DFT on the SOC-driven spin splitting in WA_2Z_4 (A = Si, Ge; Z = N, P, As) family. Our calculations are supplemented by the effective ***k.p*** model derived from the method of invariants. The calculations reveal the PST in the whole region of BZ in a single layer of these materials. The full zone persistent spin texture (FZPST) is protected by the surface inversion symmetry (SIS) $\{(x,y,z) \rightarrow (x,y,-z)\}$. In addition to spin-valley locked splitting around the corners of the BZ, we observe a cubic splitting around the center of the BZ. Significant splitting around the M point is linear in ***k***, which is found to be complementary to the linear Rashba and Dresselhaus effects. It is a well-known fact that SIS hinders the conventional linear Rashba spin splitting which is later observed under the application of out-of-plane electric field. The ***k.p*** analysis shows that PST along the M−K path is robust to the external electric field. It is generally expected that the presence of inversion symmetry in the bulk WSi_2N_4 causes the spin splitting and polarization to vanish. However, our calculations show the 100% spin polarization of doubly degenerate bands in centrosymmetric bulk and even layered WSi_2N_4, which are spatially segregated. We demonstrate that such hidden spin polarization arises by the inversion asymmetric site point group of the W atom. Thus, the WA_2Z_4 family broaden the range of currently useful materials in the fields of spintronics and valleytronics.

The geometry optimization and electronic structures are obtained using first-principles plane-wave calculations via DFT as implemented in the Vienna *ab initio* simulation package (VASP).[40] The projector augmented wave (PAW)[41,42] method and plane waves with an energy cutoff of 600 eV are incorporated. The generalized gradient algorithm includes exchange and correlation effects using Perdew−Burke−Ernzerhof (PBE)[43] functional. The electronic band structure results are further checked by using the hybrid Heyd-Scuseria-Ernzerhof (HSE06)[44] functional and G_0W_0@PBE[45,46] method. The SOC is considered in all the calculations self-consistently. BZ is sampled using Monkhorst−Pack[47] mesh of 15 × 15 × 1 and 21 × 21 × 1 for geometry optimization and self-consistent calculations, respectively. The convergence criterion for energy is set to 10^{-6} eV. In order to remove spurious interaction between periodically repeated 2D layers, a vacuum slab of 20 Å is inserted along the *z*-axis. At the same time, to consider the vdW interaction between two layers, the Tkatchenko-Scheffler[48] method with iterative Hirshfeld partitioning is used. The structures are fully relaxed using the conjugate gradient method until the maximum force on every atom is smaller than 1 meV/Å. The dynamical stabilities are calculated using density functional perturbation theory (DFPT) using PHONOPY[49] code with a supercell of 3 × 3 × 1. The dipole layer method introduces an electric field, and dipole moments are calculated using the Berry phase method.[50] We determine the optical properties by considering the many-body perturbation theory (MBPT). Dielectric functions are computed by solving the Bethe-Salpeter equation (BSE)[51] on top of G_0W_0@(PBE+SOC).

The top and side views of the optimized crystal structure of WA_2Z_4 monolayers are shown in Figure 1(a) and 1(b), which

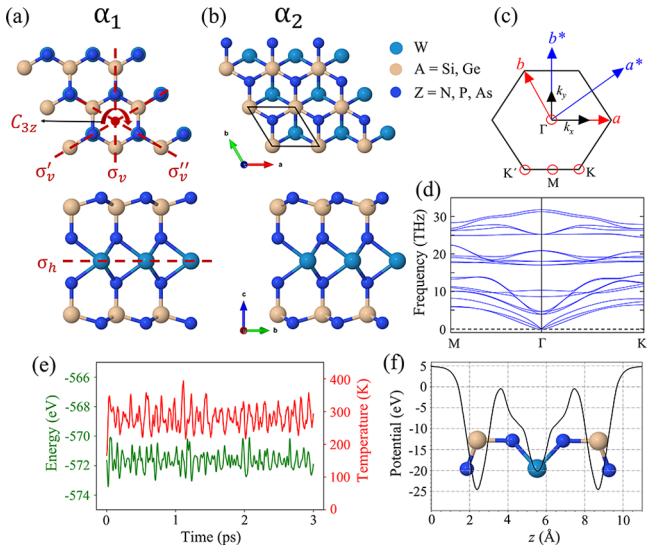

Figure 1. Crystal structures of (a) α_1- and (b) α_2-WA_2Z_4 monolayers with symmetry operations highlighted using red dashed line. The solid black lines indicate the corresponding unit cell. (c) The first BZ and the high symmetry ***k***-points (Γ, M, K, and K′) are indicated using red circles. (d) The phonon band dispersions of α_2-WSi_2N_4 monolayer. (e) Variation of total energy and temperature for α_2-WSi_2N_4 monolayer during AIMD simulation for 3 ps at 300 K. (f) Planar average of the electrostatic potential energy of the α_2-WSi_2N_4 monolayer as a function of out-of-plane axis.

can be viewed as the WZ_2 layer sandwiched between two A−Z bilayers. Depending on the stacking of A−Z bilayers, different types of crystal structures are possible. Many layered materials are influenced by these stacking effects.[29] In our work, we have considered the two most stable phases, i.e., α_1 and α_2, which differ by the position of N atoms. These two phases share the same hexagonal lattice structure with space group $P\bar{6}m2$. The associated point group symmetry is D_{3h}, containing identity operation (E), 3-fold rotation (C_{3z}) having z as the principal axis, and mirror operations perpendicular to principal axis (σ_h) and parallel to principal axis (σ_v) (see Figure 1(a)). The optimized lattice constants of WA_2Z_4 monolayers are provided in Table 1. As expected, the lattice constants increase with increasing atomic number of the group IV and V atoms. Thus, WSi_2N_4 and WGe_2As_4 exhibit the smallest and largest lattice constants, i.e., 2.88 and 3.63 Å, respectively. The same coordination environment in α_1 and α_2 structures leads to slightly different lattice constants (within 0.5%). Our lattice

https://doi.org/10.1021/acs.jpclett.2c03108
J. Phys. Chem. Lett. 2023, 14, 1494−1503

Table 1. Optimized Lattice Constant ($a = b$) of the Unit Cell of WA_2Z_4 Monolayers[a]

	Phase	a (Å)	E_{for} (eV)	P_y (eÅ)	E_g^{PBE} (eV)	$E_g^{PBE+SOC}$ (eV)	E_g^{HSE} (eV)	$E_g^{HSE+SOC}$ (eV)	E_g^{GW} (eV)
WSi_2N_4	α_1	2.881	−0.746	1.77	2.33	2.32	3.11	3.09	3.78
	α_2	2.894	−0.772	1.80	2.08	2.06	2.69	2.64	3.36
WGe_2N_4	α_1	2.976	−0.532	1.82	1.68	1.64	2.13	2.05	2.76
	α_2	2.988	−0.543	1.83	1.33	1.31	1.76	1.71	2.38
WSi_2P_4	α_1	3.413	−0.265	2.03	0.94	0.69	1.22	0.85	1.37
	α_2	3.423	−0.252	2.04	0.55	0.32	0.87	0.76	0.93
WGe_2P_4	α_1	3.486	−0.292	2.31	0.70	0.45	0.94	0.56	1.02
	α_2	3.498	−0.273	2.32	0.47	0.23	0.74	0.38	0.73
WSi_2As_4	α_1	3.561	−0.079	2.11	0.78	0.52	1.03	0.60	1.02
	α_2	3.575	−0.060	2.13	0.50	0.22	0.77	0.39	0.67
WGe_2As_4	α_1	3.624	−0.019	2.39	0.60	0.33	0.85	0.38	0.79
	α_2	3.632	−0.017	2.40	0.45	0.16	0.70	0.37	0.63

[a]Also shown, the calculated formation energy per atom (E_{for}), dipole moment per unit cell (P_y), band gaps without and with SOC using PBE (E_g^{PBE}, $E_g^{PBE+SOC}$) and HSE06 ($E_g^{HSE+SOC}$, $E_g^{HSE+SOC}$); the calculated band gaps using G_0W_0 performed on top of PBE functional with inclusion of SOC (E_g^{GW}).

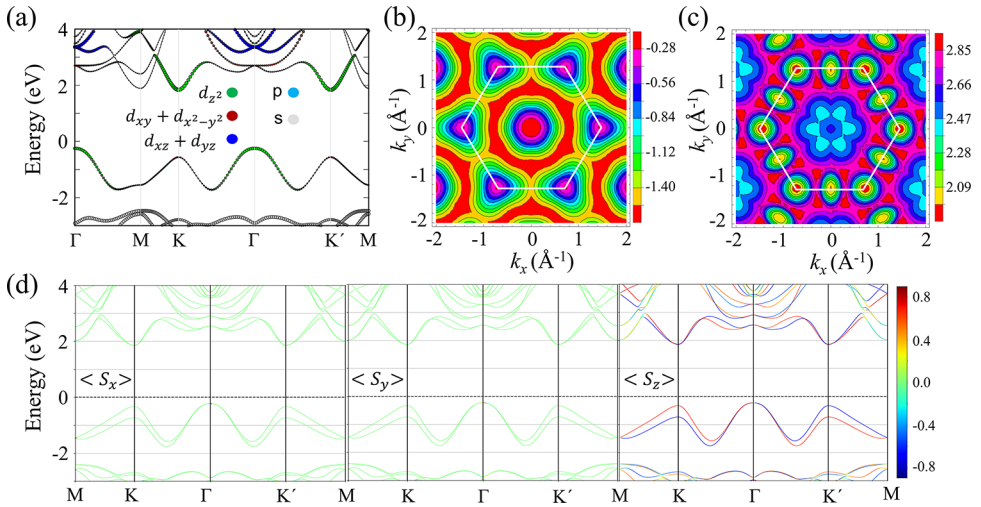

Figure 2. (a) Orbital-resolved electronic band structure of α_2-WSi_2N_4 monolayer without including SOC. Symbol size is proportional to the particular orbital weightage. The constant energy contours of (b) topmost valence band and (c) lowest conduction band in the momentum-space. The white hexagon is the first BZ. (d) Spin-resolved electronic band structure of α_2-WSi_2N_4 monolayer. The color bar shows the *x*-, *y*-, and *z*-components of spin polarization.

constants are in good agreement with already reported experimental and theoretical studies.[17,18,20,21,39]

To confirm the energy feasibility of WA_2Z_4 monolayers, the formation energy per atom (E_{for}) is calculated as follows

$$E_{for} = \{E_{tot} - (n_W E_W + n_A E_A + n_Z E_Z)\}/(n_W + n_A + n_Z) \quad (1)$$

where E_{tot} is the total ground state energy of WA_2Z_4 monolayer. E_W, E_A, and E_Z are the chemical potentials of isolated W, A, and Z atoms, respectively. n_W, n_A, and n_Z are the total number of W, A, and Z atoms in the unit cell, respectively. As seen from Table 1, the negative value of E_{for} shows the energy feasibility of WA_2Z_4 monolayers. The WA_2N_4 is most stable in the α_2 phase, while the α_1 phase has the lowest energy in the case of WA_2P_4 and WA_2As_4, which is consistent with the previous reports.[18] However, some previous studies concern only the α_2-phase for WA_2P_4 and WA_2As_4.[20,21,39] Therefore, the complete analysis of both phases is a more realistic approach. Further, to examine the dynamical stability, we have plotted the phonon dispersion plots for the concerned compounds (see Figure 1(d)). The unit cell of the WA_2Z_4 monolayer consists of seven atoms (see Figure 1(b)). As a consequence, phonon plots show three acoustic and 18 optical branches. As the general property of 2D materials, quadratic dispersion is found in out-of-plane ZA mode around the Γ point. The absence of imaginary frequencies in phonon plots confirms the dynamical stability of the WA_2Z_4 monolayers. To further check the room temperature stability, *ab initio* molecular dynamics (AIMD) simulations are performed at 300 K for 3 ps with a time step of 1 fs (see Figure 1(e)). The resultant small energy, temperature fluctuations, and no structural disruption, confirm the thermal stability of the WA_2Z_4 monolayers.

Polarization properties play a critical role in determining the intrinsic electronic properties, therefore, we investigate these effects in WA_2Z_4. First, charge transfer using Bader techniques is performed. Significant charge transfer is found in these monolayers, where Z atoms receive charge from W and A atoms. Different electronegativities lead to different amounts of charge received by different Z atoms. For instance, outer N gets a charge of 2.23 e^- from Si, whereas As receives only 0.75

https://doi.org/10.1021/acs.jpclett.2c03108
J. Phys. Chem. Lett. 2023, 14, 1494−1503

e^-. Due to SIS, charge transfer is the same for the innermost and outermost layers. Therefore, the planar average electrostatic potential shown in Figure 1(f) is symmetric along the z-direction, centering W atom. Furthermore, the only in-plane electric dipole moment (along y-direction) is observed (see Table 1).

The physics in WA_2Z_4 monolayers is essentially the same, therefore, taking α_2-WSi_2N_4 as a representative, we investigate the electronic properties of this class of materials. Figure 2(a) shows the orbital-projected electronic band structure of α_2-WSi_2N_4 without SOC calculated using the GGA-PBE functional. It has an indirect band gap of 2.08 eV, which is consistent with the previous findings.[17,18,21,39] The W-d orbitals dominate the states near the band edges. The valence band maximum (VBM) at Γ and conduction band minimum (CBm) at K point mainly consist of d_{z^2} orbitals, whereas, d_{xy} and $d_{x^2-y^2}$ contribute to the top valence states at the K/K′ point. To clearly visualize these two bands, constant energy contours are plotted in momentum-space, as shown in Figure 2(b) and 2(c). It is found that the energies near CBm and VBM are elliptically wrapped. On the other hand, energies are triangularly wrapped for the valence band around the K/K′ point, similar to the MoS_2 family.[31] In addition to WSi_2N_4, WGe_2N_4 also has an indirect band gap with band edge positions similar to WSi_2N_4. On the contrary, WA_2P_4 and WA_2As_4 have a direct band gap at the K/K′ point (see sections I and II of Supporting Information (SI)).

When SOC is included, as seen in Figure 2(d), the band structure is strongly modified and a sizable spin splitting is observed throughout the BZ, which is the consequence of intrinsic inversion symmetry breaking. The band gap of α_2-WSi_2N_4 decreases to 2.06 eV owing to the SOC induced spin splitting. As PBE is known to underestimate the electronic band gap, the band structures are also calculated using a more sophisticated functional HSE06 and G_0W_0 approach (see sections I and II of the SI). The values of band gaps using different functionals are compared in Table 1. To appraise the optical absorption of WSi_2N_4, we calculate the real and imaginary parts of the dielectric tensor. The dielectric tensor (ϵ) is isotropic in plane due to the D_{3h} point group symmetry (see section II of SI). Therefore, we consider only the ϵ_{xx} by performing BSE calculation on top of G_0W_0@PBE+SOC as shown in Figure S4. The first absorption peak is observed at 2.49 eV, therefore, it is responsive to the energy spectrum in the visible region.

The transport properties of electrons are mainly governed by the conduction and valence bands. Figure 3 shows the magnitude of spin splitting energy ($\Delta E = |E(\boldsymbol{k}, \uparrow) - E(\boldsymbol{k}, \downarrow)|$) for the topmost valence bands and lowest conduction bands in the entire momentum-space. Splitting present in the valence band is significantly larger as compared to the conduction band. For this reason, we mainly focus on the valence bands. The splitting is observed in the full BZ except for the high symmetry path Γ − M, where the eigenstates are at least 2-fold degenerate. The degenerate bands split around the time-reversal invariant Γ and M points. Importantly, the splitting observed around the M and Γ point is anisotropic in nature. The maximum spin splitting energy observed around the M point is 35 meV along the M−K line, which mainly originates from the strong hybridization of d_{xy} and $d_{x^2-y^2}$ orbitals. Similar features of spin splitting are also observed in the whole WA_2Z_4 family (see Figure S1 in SI). The DFT results are further examined using symmetry analysis.

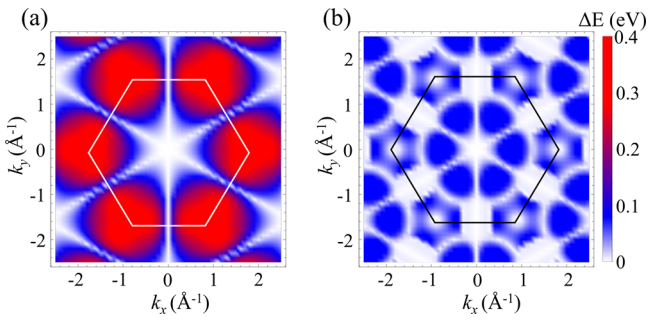

Figure 3. Spin splitting energy ($\Delta E = |E(k, \uparrow) - E(k, \downarrow)|$) for (a) topmost valence band and (b) lowest conduction band mapped over the full BZ.

To better understand the spin splitting properties, we have constructed the 2-band ***k.p*** model using the method of invariants, which describes the dispersion around Γ, M, and K points. The minimal ***k.p*** model is derived by including the spin degrees of freedom. Therefore, we have chosen eigenstates of Pauli matrix σ_z, $|\uparrow\rangle$ and $|\downarrow\rangle$ with eigenvalues +1 and −1, respectively, as the basis set. The little group of Γ point is D_{3h}. The symmetry allowed Hamiltonian considering the terms up to third order in momentum reads as[52] (see section III of SI)

$$H_\Gamma(\boldsymbol{k}) = H_0(\boldsymbol{k}) + \lambda k_x(3k_y^2 - k_x^2)\sigma_z \tag{2}$$

where $H_0(\boldsymbol{k})$ is the free part of the Hamiltonian having energy eigenvalues $E_0(\boldsymbol{k}) = \frac{\hbar^2 k_x^2}{2m_x^*} + \frac{\hbar^2 k_y^2}{2m_y^*}$. Here, m_x^* and m_y^* are the effective masses along k_x and k_y directions, respectively. The lowest order symmetry allowed splitting term is cubic in $\boldsymbol{k}$. Around the Γ point, bands split along k_x (Γ−K) direction and doubly degenerate along k_y (Γ−M) direction. On the other hand, the little group of M point is C_s, containing the σ_h and σ_v operations. The effective ***k.p*** model for band dispersion around the M point is given by (see section III of SI)

$$H_M(\boldsymbol{k}) = H_0(\boldsymbol{k}) + \alpha k_x \sigma_z \tag{3}$$

The splitting is linear in $\boldsymbol{k}$ around the M point and can be treated as complementary to linear Rashba or linear Dresselhaus. In addition, the splitting is strongly anisotropic in nature, i.e., bands are degenerate along the k_y (M−Γ) direction and are lifted along the k_x (M−K) direction. At the K/K′ point, the associated little group is C_{3h}. Thus, the ***k.p*** model is given by (see section III of SI)

$$H_K(\boldsymbol{k}) = H_0(\boldsymbol{k}) + k_x(3k_y^2 - k_x^2) + \sigma_z[\Delta + \eta(k_x^2 + k_y^2) + \zeta k_x(3k_y^2 - k_x^2)] \tag{4}$$

At the K/K′ point, Zeeman-type splitting in the valence band is predicted by the nonzero coefficient Δ in $H_K(\boldsymbol{k})$. The Δ observed for time-reversal conjugate valleys K/K′ is the same, whereas, the nature of spin splitting is opposite in nature. The properties which are odd under the time-reversal will have an opposite nature at K and K′ valleys. The spin polarization is one such feature (see Figure 2(d)). Hence, the spin degrees of freedom and valleys are distinctly locked at inequivalent valleys. Therefore, the flip of only one binary index is forbidden. This strong coupling between spin and valley may enable the long-life valley and spin relaxation.

https://doi.org/10.1021/acs.jpclett.2c03108
J. Phys. Chem. Lett. 2023, 14, 1494−1503

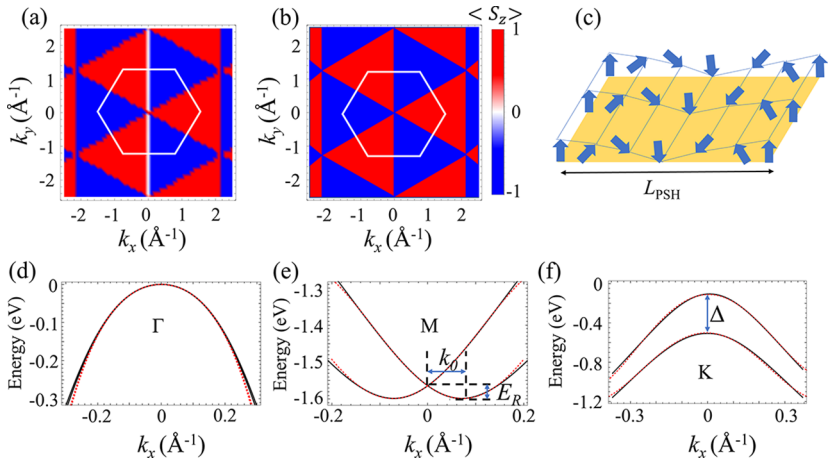

Figure 4. Spin textures of topmost valence bands associated with the outer branch using (a) DFT and (b) ***k.p*** models. The energy of the outer branch is smaller or equal as compared to the energy of inner branch at the ***k***-point in the considered range. The color bar shows the out-of-plane (z-) component of spin textures. (c) Schematic diagram of PSH state. The L_{PSH} represents the wavelength of spatially periodic mode. The band structure of topmost valence bands around (d) Γ, (e) M, and (f) K points. Here, the black solid lines and red dots represent the band structure computed using DFT and ***k.p*** models, respectively.

Figure 4(a) and 4(b) show the spin textures computed using DFT and ***k.p*** models, respectively. It is clearly seen that in-plane spin components are absent and band dispersion is fully characterized by the out-of-plane spin component. The spin polarization of Bloch states is either parallel or antiparallel to the z-direction leading to the case of PST. These spin textures are different from widely reported locally existing persistent spin textures and are preserved in the whole BZ.[53−56] Therefore, the control of Fermi level to a specific part of BZ where PST occurs is not required. These full-zone persistent spin textures (FZPST) can be explained using the symmetry arguments. The little group of the arbitrary ***k***-point is C_s containing the σ_h operation, besides the trivial identity. This imparts a condition on the spin expectation values at an arbitrary ***k***-point as follows:

$$\sigma_h^{-1} s(\boldsymbol{k}) = s(\boldsymbol{k}) \tag{5}$$

and therefore

$$(S_x, S_y, S_z) = (-S_x, -S_y, S_z) \tag{6}$$

This condition is satisfied only when the in-plane spin components are zero, leading to FZPST along the z-direction. This is in accordance with DFT and ***k.p*** model predictions. The SOC part of Hamiltonian can be written as, $H_{SOC}(\boldsymbol{k}) = \Omega(\boldsymbol{k}).\sigma$, where $\Omega(\boldsymbol{k})$ is the spin−orbit field (SOF). In the present case, electron motion accompanied by the spin precession around the unidirectional SOF. This leads to a spatially periodic mode of spin polarization, forming a highly stable persistent spin helix (PSH) state.[34] The SU(2) conservation laws in the PSH state imply that the spin expectation values have an infinite lifetime.[57] Since S_z is a conserved quantity, the fluctuation in the z-component of spin polarization with wave vector can only decay by diffusion, thus protecting the spins from dephasing. Figure 4(c) shows the schematic diagram of PSH, where L_{PSH} is the wavelength of PSH. The angular frequency (ω) of precession around SOF can be expressed as $\omega = -\gamma B$, where γ is the gyromagnetic ratio. The magnitude of the effective magnetic field can be expressed in terms of the spin−orbit field as $B = 2|\Omega|/\gamma\hbar$.[34] For the Rashba-Dresselhaus-like dispersed bands around the M point, $|\Omega| = \alpha k_x$ (see eq 3). Therefore, the magnetic field takes the expression $B = 2\alpha k_x/\gamma\hbar$. The spin precession angle (θ) around the y-axis for an electron moving in real space, under the influence of unidirectional SOF at the time t is $\theta = \omega t = 2\alpha k_x t/\hbar$. The time at which precession completes a revolution ($\theta = 2\pi$) is $t = \pi\hbar/\alpha k_x$. The distance traveled by the electron along y-axis in this time period is $L_{PSH} = vt = \hbar k_x t/m^*$. Therefore, the PSH length is given by

$$L_{PSH} = \frac{\pi\hbar^2}{m^*\alpha} \tag{7}$$

The length of PSH mode can be calculated by evaluating the band dispersion parameters m^* and α. The PSH mechanism leads to the long-range spin transport without dissipation, enabling better efficiency in spintronics devices. In order to quantify the strength of splitting effects, we parametrize the splitting coefficients (λ, α, Δ, η, and ζ) by fitting the DFT band structures. In general, we are interested in coefficients having the largest contribution in band splitting, i.e., λ, α, and Δ. Figure 4(d)−(f) show the comparison between the DFT and model resulted band splits. The splitting observed around the Γ point is very tiny (λ = 0.21 eV Å^3), as the energy contribution coming from the term cubic in ***k*** is very small, i.e., $k_x \ll 1$ Å. The linear splitting observed around the M point is α = 0.92 eV Å. The energy eigenvalues of the ***k.p*** model given in eq 3 can be written as

$$E_M^{\pm} = \frac{\hbar^2}{2m^*}(|\boldsymbol{k}| \pm k_0)^2 + E_R \tag{8}$$

where E_R and k_0 are the shifting energy and wave vector, respectively, calculated from the spin-split bands along the k_x (Γ − K) direction as shown in Figure 4(e). The α can also be estimated using E_R and k_0 as follows

$$\alpha = \frac{2E_R}{k_0} \tag{9}$$

The values of E_R = 35 meV and k_0 = 0.075 Å lead to α = 0.93 eV Å. In addition, we calculate the L_{PSH} from the eq 7, and it is found to be 4.84 nm for α_2-WSi_2N_4. Table 2 shows the calculated values of α, Δ, and L_{PSH} for the WA_2Z_4 family. The effect of SOC increases with increasing atomic weight,

https://doi.org/10.1021/acs.jpclett.2c03108
J. Phys. Chem. Lett. 2023, 14, 1494−1503

Table 2. Calculated SOC Parameters, viz. α, Δ, and Wavelength of PSH Mode (L_{PSH}) of Upper Valence Bands for the WA_2Z_4 Family

	phase	α (eV Å)	Δ (eV)	L_{PSH} (nm)
WSi_2N_4	α_1	0.87	0.384	5.03
	α_2	0.92	0.397	4.84
WGe_2N_4	α_1	1.20	0.435	4.51
	α_2	1.21	0.437	4.49
WSi_2P_4	α_1	1.19	0.407	4.42
	α_2	1.22	0.429	4.31
WGe_2P_4	α_1	1.37	0.450	4.08
	α_2	1.33	0.442	4.07
WSi_2As_4	α_1	1.47	0.459	3.99
	α_2	1.61	0.496	3.21
WGe_2As_4	α_1	1.74	0.499	3.16
	α_2	1.79	0.507	2.89

therefore, the splitting is in the order Ge > Si and As > *P* > N. The observed values of α are larger than traditional TMDs (0.05−0.40 eV Å),[58] WO_2Cl_2 monolayer (0.90 eV Å),[59] defective $PtSe_2$ (0.20−1.14 eV Å),[60] and $(Mo,W)X_2$ (X = S,Se)(0.14−0.26 eV Å) .[61]

An external electric field (EEF) is always considered as an effective approach to manipulate and introduce new splittings by breaking the inversion symmetry, without changing the time-reversal invariant symmetry.[62,63] Previous studies have shown that the strength of Rashba-type splitting is tunable with the help of EEF.[58,64] To understand the effect of EEF, we theoretically apply the EEF in the range of 0 to 0.5 V/Å, in the *z*-direction on α_2−WSi_2N_2, as illustrated in Figure 5(a). First, we plot the planar average of the electrostatic potential energy as a function of *z*. In contrast to the case without EEF, the potential energy here is asymmetric with respect to the W atom (see Figure 5(b)). It can be easily seen that a significant potential difference (δV = 2.3 eV) is generated between the two Si-layers. The potential energy on the upper side of the Si layer is larger compared to its lower counterpart. This confirms the breaking of the SIS. Then, we observe the effect of EEF on band gaps, which can be explained as the stark effect in a condensed matter system. Our system is out-of-plane symmetric, therefore, EEF shows the same effect in both positive and negative *z*-directions. Figure 5(c) shows the band gap variation as a function of EEF. Between 0.1 and 0.2 V/Å, the position of CBm changes from the K point to the M point (see Figure S5 in SI). The band gap is nearly constant up to 0.2 V/Å and thereafter, decreases linearly to 1.59 eV under 0.5 V/Å EEF. Figure 5(d) shows the spin projected band structure with an EEF of 0.5 V/Å. Here, we see that near VBM (Γ point), the out-of-plane spin component vanishes and the in-plane spin components arise. Figure 6(a) and 6(b) show the

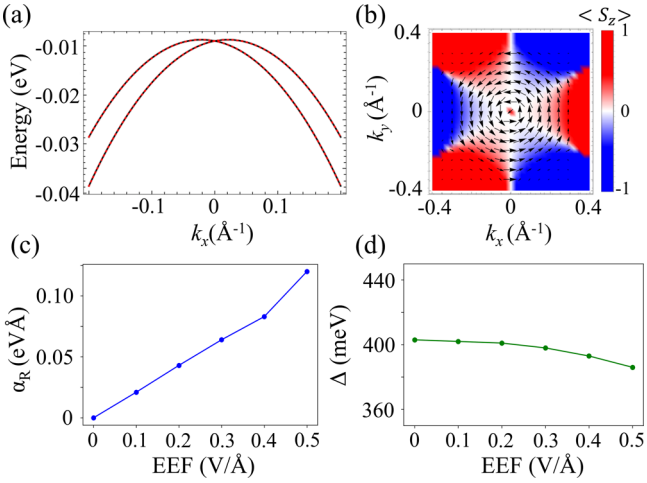

Figure 6. (a) The topmost valence bands and the associated (b) spin texture around the Γ point for the α_2-WSi_2N_4 monolayer. The black solid lines and red dots represent the band structure computed using DFT and the ***k.p*** model, respectively. The arrows and color bar show the in-plane (*x*- and *y*-) and out-of-plane (*z*-) components of spin texture, respectively. The variation of (c) α_R and (d) Δ as a function of EEF.

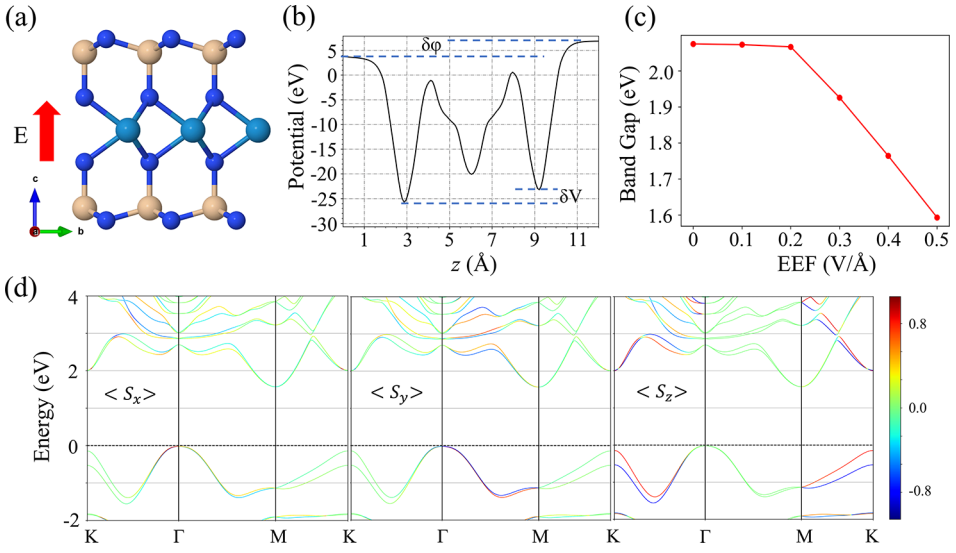

Figure 5. Direction of EEF shown with respect to the side view of α_2-WSi_2N_4. (b) The planar average electrostatic potential under the application of EEF as a function of out-of-plane axis. Here, δV denotes the electrostatic potential difference between two Si layers and $\delta\phi$ denotes the workfunction difference between two outer surfaces. (c) Variation of the band gap as a function of EEF. (d) The spin-projected band structure under the EEF of strength 0.5 V Å. The color bar shows the *x*-, *y*-, and *z*- components of spin polarization.

https://doi.org/10.1021/acs.jpclett.2c03108
J. Phys. Chem. Lett. 2023, 14, 1494−1503

band structure around Γ point and associated spin texture, respectively. The helical-type in-plane spin polarization confirms the existence of Rashba-type splitting.

To understand Rashba splitting, we include an additional EEF dependent term in the aforementioned ***k.p*** models, which is given as

$$H^{\mathrm{EEF}}(\boldsymbol{k}) = \alpha_R(\sigma_x k_y - \sigma_y k_x) \tag{10}$$

where α_R is the splitting coefficient dependent on the strength of EEF. The $H^{\mathrm{EEF}}(\boldsymbol{k})$ term breaks the SIS, which reduces the point group symmetry of the 2D system from D_{3h} to C_{3v} and considers the in-plane spin component. The contribution of $H^{\mathrm{EEF}}(\boldsymbol{k})$ near the Γ point is dominant as compared to the cubic term, therefore, the in-plane spin component is observed near the Γ point. Furthermore, the out-of-plane component starts dominating as we move away from the Γ point. Figure 6(c) and 6(d) show the variation of α_R (around Γ point) and Δ as a function of EEF. The α_R is linearly dependent on the EEF. Such a linear relationship helps in the precise control of spin-precession in spin field-effect transistors. When the EEF is 0.5 V/Å, the Rashba spin splitting occurs at the Γ point with a Rashba coefficient of 0.12 eV Å, obtained by parametrizing the Hamiltonian given in eq 10. The observed values of α_R are small as compared to the TMD (α_R = 0.20 eV Å) under the same EEF, since the W atom is covered by the Si−N layers. Thus, the W-*d* orbitals contributing to the VBM are less influenced by the EEF. The spin splitting and spin textures around K and M points are hardly influenced by the EEF, because the nonzero constant term Δ around K and linear term with coefficient α dominate over the $H^{\mathrm{EEF}}(\boldsymbol{k})$. Therefore, the SOFs $\Omega_K(\boldsymbol{k})$ and $\Omega_M(\boldsymbol{k})$ are parallel to the *z*-direction and are independent of EEF. The PST preserve fully along the M−K path having only the out-of-plane component of spin polarization. Therefore, PST are robust to small EEF, except around the Γ point.

The previous theoretical study reports the possibility of experimental realization of layered bulk WSi_2N_4 family, using the bottom up synthesis method.[39] We have considered the layer dependence of the spin polarization in the layered WSi_2N_4 family. The bulk WSi_2N_4 has an indirect band gap of 1.97 eV having CBm and VBM at K and Γ, respectively.[39] Figure 7(a) shows the unit cell of bulk WSi_2N_4 having $P6_3/mmc$ space group symmetry. The associated point group symmetry is D_{6h} and has a point of inversion as shown in Figure 7(a). The presence of inversion and time reversal symmetries leads to the bands being 2-fold degenerate throughout the BZ. As expected, the top valence bands are 2-fold degenerate as shown in Figure 7(b). In the current view, the Rashba and Dresselhaus effects are observed only when the inversion symmetry is absent. Thus, it is unwise to look for spin splitting and spin polarization in centrosymmetric bulk WSi_2N_4. Therefore, the degree of spin polarization is expected to be zero in inversion symmetric even layered and bulk WSi_2N_4, as reported in ref 39. In contrast, we report the existence of hidden spin polarization for bulk WSi_2N_4, which can be attributed to the hidden Dresselhaus (D-2) effect.[65] The key point here is that SOC is anchored on particular nuclear sites in the solid, thus it is the individual atomic site symmetry in solid that forms a good starting point to describe the SOC-induced spin-polarization. The net spin polarization of the bulk crystal is the sum of the local polarization over the atomic sites. The D-2 effect arises when the site point group of

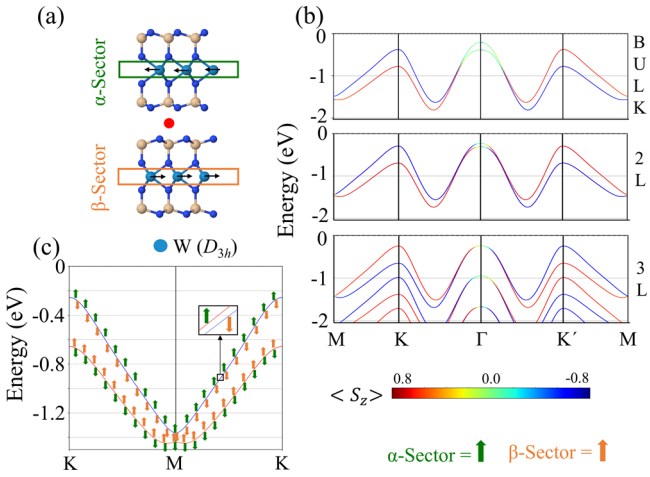

Figure 7. (a) Side view of the bulk crystal structure of WSi_2N_4 with site point group of W atom. The red dot represents the inversion center. The two boxed real-space sectors forming the inversion partners are used for spin projection and are considered as α-sector and β-sector. The black arrows on W atoms represent the direction of dipole moment on particular atomic sites. (b) The spin-projected top valence bands of bulk WSi_2N_4, bilayer (2L), and trilayer (3L). The color bar shows the out-of-plane (*z*-) component of spin textures. (c) The spin- and atom-projected band structure of top valence bands along the K−M−K path. The green and orange color shows the band is coming from α- and β-sectors, respectively. The up and down arrows show the *z*-component of spin polarization. Note that the in-plane spin components are zero along that path.

an atom within a 3D crystal lacks inversion asymmetry and the crystal as a whole is centrosymmetric.[65]

In the present case, the inversion symmetry is present in the bulk space group but not in the site point groups (see Figure 7(a)). One such atomic site is the W atom, where site point group is inversion asymmetric D_{3h}, contributing mainly to the low-energy spectrum. The two W layers connected by the inversion symmetry are indicated as sectors S_α and S_β. The two sectors are individually inversion asymmetric and produce equal dipole moment but in opposite directions (see Figure 7(a)). Therefore, the net dipole moment of bulk WSi_2N_4 becomes zero, which is the central property of centrosymmetric structures. Figure 7(c) shows the band structure projected on the spin components and real space sectors S_α and S_β. If we consider only one sector, the large band splitting (∼0.4 eV) between spin-up and spin-down states is observed along the K−M−K path. The interactions between the sectors form a pair of bonding and antibonding states, and therefore, open a band gap at the band crossing M point.[66] Even though the bands are doubly degenerate as a consequence of bulk inversion asymmetry, the branches of doubly degenerate bands have opposite spin polarizations, which are separated in the real space (see Figure 7(c)). As already discussed, S_z is a good quantum number, therefore, the spins are fully out-of-plane and up and down spins locate at the energy bands. The weak van der Waals interaction among inversion partners causes slight spin mixture from another layer and slightly larger separation of the degenerate bands. However, most of the spin at the K valley remains on each layer. The real space segregation of spin polarized bands originates from the separate local sites Dresselhaus SOC. The bulk spin polarization in such systems can be observed by controlling the stacking directions probing beams.[67−69] The extra advantage of

https://doi.org/10.1021/acs.jpclett.2c03108
J. Phys. Chem. Lett. 2023, 14, 1494−1503

the D-2 effect is that the spins can be controlled by manipulating the interaction between two inversion parts. One such example is that a small electric field (∼1 mV/Å) is required to reverse the spin polarization as compared to the linear Rashba effect.[70]

The results similar to the bulk are expected to be observed for an even number of layers of WSi_2N_4, having centrosymmetric $P6_3/mmc$ space group symmetry. Therefore, we have examined the results for bilayer-WSi_2N_4. The real space segregated hidden spin polarization is also observed in doubly degenerate bands of topmost valence bands (see Figure 7(b)). The band splitting similar to monolayer is observed in odd number of layers of WSi_2N_4 having noncentrosymmetric $P\bar{6}m2$ space group symmetry (i.e., see band structure for trilayer in Figure 7(b)).

Now, let us comment on the possible applications of PST in WA_2Z_4 materials, which can act as a channel for spin-FET. The out-of-plane spin polarization is injected through the ferromagnetic source. The SOC rotate its polarization during its path, and is either transmitted or reflected to the drain electrode depending upon the spin state, therefore, acting as on or off states, respectively.[34] The on/off functionality can be further controlled by the EEF. The observed small value of L_{PSH}, i.e., 2.89 nm, is promising for highly efficient devices. The coexistence of hidden spin polarization and PST is another important avenue to pursue.

We have revealed the interesting spin splitting properties of the WA_2Z_4 family. The formation energies, phonon spectra, and AIMD calculations confirm the stability of these materials. The PBE, HSE06, and the excited state methods G_0W_0 and BSE show that these materials are semiconducting, having a band gap in the visible region. In addition to valley dependent properties at the corners of the BZ, we have observed cubic and linear split bands around the time-reversal invariant Γ and M points, respectively. The in-plane mirror symmetry (σ_h) leads to out-of-plane FZPST, therefore, enabling dissipationless long-range transport through the spatially periodic mode PSH mechanism. The effect of EEF is duly considered on band gap and spin splitting. The EEF leads to linear Rashba-type helical spin texture around the VBM. The impact of layer thickness is studied in the aforementioned effects. We have found the hidden spin polarization in the bulk and even layered WSi_2N_4, which can be attributed to the D-2 effect. The D-2 effect arises because the local site point of the W atom lacks inversion symmetry; however, the global space group is centrosymmetric. The PST is robust to electric field and thickness along the M−K direction. We believe that this work will provide highly efficient spintronics and valleytronics devices for room temperature applications.

■ ASSOCIATED CONTENT

Supporting Information

The Supporting Information is available free of charge at https://pubs.acs.org/doi/10.1021/acs.jpclett.2c03108.

(I) Electronic structure of WA_2Z_4 using PBE+SOC and HSE06+SOC. (II) Electronic and optical properties of WSi_2N_4 using beyond DFT methods. (III) The ***k.p*** models. (IV) Electric field effect on electronic structure (PDF)

■ AUTHOR INFORMATION

Corresponding Authors

Sajjan Sheoran − *Department of Physics, Indian Institute of Technology Delhi, New Delhi 110016, India;* orcid.org/0000-0002-6816-3944; Email: sajjan@physics.iitd.ac.in

Saswata Bhattacharya − *Department of Physics, Indian Institute of Technology Delhi, New Delhi 110016, India;* orcid.org/0000-0002-4145-4899; Phone: +91-2659 1359; Email: saswata@physics.iitd.ac.in; Fax: +91-2658 2037

Authors

Sanchi Monga − *Department of Physics, Indian Institute of Technology Delhi, New Delhi 110016, India*

Ankita Phutela − *Department of Physics, Indian Institute of Technology Delhi, New Delhi 110016, India*

Complete contact information is available at: https://pubs.acs.org/10.1021/acs.jpclett.2c03108

Notes

The authors declare no competing financial interest.

■ ACKNOWLEDGMENTS

S.S. acknowledges CSIR, India, for the senior research fellowship [grant no. 09/086(1432)/2019-EMR-I]. S.M. and A.P. acknowledge IIT Delhi for the junior research fellowship. S.S. acknowledges Deepika Gill for helpful discussions and careful reading of the manuscript with suggestions. S.B. acknowledges financial support from SERB under a core research grant (grant no. CRG/2019/000647) to set up his High Performance Computing (HPC) facility "Veena" at IIT Delhi for computational resources. We acknowledge the High Performance Computing (HPC) facility at IIT Delhi for computational resources.

■ REFERENCES

(1) Geim, A. K. Graphene: status and prospects. *Science* **2009**, *324*, 1530−1534.

(2) Novoselov, K. S.; Fal'ko, V. I.; Colombo, L.; Gellert, P. R.; Schwab, M. G.; Kim, K. A roadmap for graphene. *Nature* **2012**, *490*, 192−200.

(3) Kane, C. L.; Mele, E. J. Quantum spin Hall effect in graphene. *Phys. Rev. Lett.* **2005**, *95*, 226801.

(4) Mohanta, M. K.; IS, F.; Kishore, A.; De Sarkar, A. Spin-current modulation in hexagonal buckled ZnTe and CdTe monolayers for self-powered flexible-piezo-spintronic devices. *ACS Appl. Mater. Interfaces* **2021**, *13*, 40872−40879.

(5) Pei, Q.; Zhou, B.; Mi, W.; Cheng, Y. Triferroic material and electrical control of valley degree of freedom. *ACS Appl. Mater. Interfaces* **2019**, *11*, 12675−12682.

(6) Ni, Z.; Liu, Q.; Tang, K.; Zheng, J.; Zhou, J.; Qin, R.; Gao, Z.; Yu, D.; Lu, J. Tunable bandgap in silicene and germanene. *Nano Lett.* **2012**, *12*, 113−118.

(7) Molle, A.; Grazianetti, C.; Tao, L.; Taneja, D.; Alam, M. H.; Akinwande, D. Silicene, silicene derivatives, and their device applications. *Chem. Soc. Rev.* **2018**, *47*, 6370−6387.

(8) Chopra, N. G.; Luyken, R.; Cherrey, K.; Crespi, V. H.; Cohen, M. L.; Louie, S. G.; Zettl, A. Boron nitride nanotubes. *Science* **1995**, *269*, 966−967.

(9) Golberg, D.; Bando, Y.; Tang, C.; Zhi, C. Boron nitride nanotubes. *Adv. Mater.* **2007**, *19*, 2413−2432.

(10) Ullah, F.; Lee, J.-H.; Tahir, Z.; Samad, A.; Le, C. T.; Kim, J.; Kim, D.; Rashid, M. U.; Lee, S.; Kim, K.; Cheong, H.; Jang, J. I.; Seong, M.-J.; Kim, Y. S. Selective Growth and Robust Valley

Polarization of Bilayer 3R-MoS2. *ACS Appl. Mater. Interfaces* **2021**, *13*, 57588−57596.
(11) Manzeli, S.; Ovchinnikov, D.; Pasquier, D.; Yazyev, O. V.; Kis, A. 2D transition metal dichalcogenides. *Nat. Rev. Mater.* **2017**, *2*, 1−15.
(12) Xu, X.; Yao, W.; Xiao, D.; Heinz, T. F. Spin and pseudospins in layered transition metal dichalcogenides. *Nat. Phys.* **2014**, *10*, 343−350.
(13) Wang, G.; Chernikov, A.; Glazov, M. M.; Heinz, T. F.; Marie, X.; Amand, T.; Urbaszek, B. Colloquium: Excitons in atomically thin transition metal dichalcogenides. *Rev. Mod. Phys.* **2018**, *90*, 021001.
(14) Li, H.; Shao, J.; Yao, D.; Yang, G. Gate-voltage-controlled spin and valley polarization transport in a normal/ferromagnetic/normal MoS2 junction. *ACS Appl. Mater. Interfaces* **2014**, *6*, 1759−1764.
(15) Shuck, C. E.; Sarycheva, A.; Anayee, M.; Levitt, A.; Zhu, Y.; Uzun, S.; Balitskiy, V.; Zahorodna, V.; Gogotsi, O.; Gogotsi, Y. Scalable synthesis of $Ti_3C_2T_x$ mxene. *Adv. Energy Mater.* **2020**, *22*, 1901241.
(16) Zhan, X.; Si, C.; Zhou, J.; Sun, Z. MXene and MXene-based composites: synthesis, properties and environment-related applications. *Nanoscale Horiz* **2020**, *5*, 235−258.
(17) Hong, Y.-L.; Liu, Z.; Wang, L.; Zhou, T.; Ma, W.; Xu, C.; Feng, S.; Chen, L.; Chen, M.-L.; Sun, D.-M.; Chen, X.-Q.; Cheng, H.-M.; Ren, W. Chemical vapor deposition of layered two-dimensional $MoSi_2N_4$ materials. *Science* **2020**, *369*, 670−674.
(18) Wang, L.; Shi, Y.; Liu, M.; Zhang, A.; Hong, Y.-L.; Li, R.; Gao, Q.; Chen, M.; Ren, W.; Cheng, H.-M.; Li, Y.; Chen, X.-Q. Intercalated architecture of MA_2Z_4 family layered van der Waals materials with emerging topological, magnetic and superconducting properties. *Nat. Commun.* **2021**, *12*, 1−10.
(19) Yang, J.-S.; Zhao, L.; LI, S.-Q.; Liu, H.; Wang, L.; Chen, M.; Gao, J.; Zhao, J. Accurate electronic properties and non-linear optical response of two-dimensional MA_4Z_4. *Nanoscale* **2021**, *13*, 5479−5488.
(20) Yang, C.; Song, Z.; Sun, X.; Lu, J. Valley pseudospin in monolayer $MoSi_2N_4$ and $MoSi_2As_4$. *Phys. Rev. B* **2021**, *103*, 035308.
(21) Huang, D.; Liang, F.; Guo, R.; Lu, D.; Wang, J.; Yu, H.; Zhang, H. $MoSi_2N_4$: A 2D Regime with Strong Exciton−Phonon Coupling. *Adv. Opt. Mater.* **2022**, *10*, 2102612.
(22) Mortazavi, B.; Javvaji, B.; Shojaei, F.; Rabczuk, T.; Shapeev, A. V.; Zhuang, X. Exceptional piezoelectricity, high thermal conductivity and stiffness and promising photocatalysis in two-dimensional $MoSi_2N_4$ family confirmed by first-principles. *Nano Energy* **2021**, *82*, 105716.
(23) Priydarshi, A.; Chauhan, Y. S.; Bhowmick, S.; Agarwal, A. Large and anisotropic carrier mobility in monolayers of the MA_2Z_4 series (M= Cr, Mo, W; A= Si, Ge; Z= N, P). *Nanoscale* **2022**, *14*, 11988.
(24) Hussain, G.; Samad, A.; Rehman, M. U.; Cuono, G.; Autieri, C. Emergence of Rashba splitting and spin-valley properties in Janus $MoGeSiP_2As_2$ and $WGeSiP_2As_2$ monolayers. *J. Magn. Magn. Mater.* **2022**, *563*, 169897.
(25) Yin, Y.; Gong, Q.; Yi, M.; Guo, W. Emerging versatile two-dimensional $MoSi_2N_4$ family. *arXiv* **2022**, No. 2211.00827.
(26) Pacchioni, G. Valleytronics with a twist. *Nat. Rev. Mater.* **2020**, *5*, 480−480.
(27) Kang, J.; Li, J.; Li, S.-S.; Xia, J.-B.; Wang, L.-W. Electronic structural Moiré pattern effects on $MoS_2/MoSe_2$ 2D heterostructures. *Nano Lett.* **2013**, *13*, 5485−5490.
(28) Singh, S.; Espejo, C.; Romero, A. H. Structural, electronic, vibrational, and elastic properties of graphene/MoS_2 bilayer heterostructures. *Phys. Rev. B* **2018**, *98*, 155309.
(29) He, J.; Hummer, K.; Franchini, C. Stacking effects on the electronic and optical properties of bilayer transition metal dichalcogenides MoS_2, $MoSe_2$, WS_2, and WSe_2. *Phys. Rev. B* **2014**, *89*, 075409.
(30) Lin, C.; Li, Y.; Wei, Q.; Shen, Q.; Cheng, Y.; Huang, W. Enhanced valley splitting of transition-metal dichalcogenide by vacancies in robust ferromagnetic insulating chromium trihalides. *ACS Appl. Mater. Interfaces* **2019**, *11*, 18858−18864.
(31) Xiao, D.; Liu, G.-B.; Feng, W.; Xu, X.; Yao, W. Coupled spin and valley physics in monolayers of MoS_2 and other group-VI dichalcogenides. *Phys. Rev. Lett.* **2012**, *108*, 196802.
(32) Schmidt, H.; Yudhistira, I.; Chu, L.; Castro Neto, A. H.; Ozyilmaz, B.; Adam, S.; Eda, G. Quantum transport and observation of Dyakonov-Perel spin-orbit scattering in monolayer MoS_2. *Phys. Rev. Lett.* **2016**, *116*, 046803.
(33) Ochoa, H.; Castro Neto, A. H.; Guinea, F. Elliot-Yafet mechanism in graphene. *Phys. Rev. Lett.* **2012**, *108*, 206808.
(34) Schliemann, J. Colloquium: Persistent spin textures in semiconductor nanostructures. *Rev. Mod. Phys.* **2017**, *89*, 011001.
(35) Tao, L.; Tsymbal, E. Y. Persistent spin texture enforced by symmetry. *Nat. Commun.* **2018**, *9*, 1−7.
(36) Zhao, H. J.; Nakamura, H.; Arras, R.; Paillard, C.; Chen, P.; Gosteau, J.; Li, X.; Yang, Y.; Bellaiche, L. Purely Cubic Spin Splittings with Persistent Spin Textures. *Phys. Rev. Lett.* **2020**, *125*, 216405.
(37) Li, S.; Wu, W.; Feng, X.; Guan, S.; Feng, W.; Yao, Y.; Yang, S. A. Valley-dependent properties of monolayer $MoSi_2N_4$, WSi_2N_4, and $MoSi_2As_4$. *Phys. Rev. B* **2020**, *102*, 235435.
(38) Ai, H.; Liu, D.; Geng, J.; Wang, S.; Lo, K. H.; Pan, H. Theoretical evidence of the spin−valley coupling and valley polarization in two-dimensional $MoSi_2X_4$ (X= N, P, and As). *Phys. Chem. Chem. Phys.* **2021**, *23*, 3144−3151.
(39) Islam, R.; Ghosh, B.; Autieri, C.; Chowdhury, S.; Bansil, A.; Agarwal, A.; Singh, B. Tunable spin polarization and electronic structure of bottom-up synthesized $MoSi_2N_4$ materials. *Phys. Rev. B* **2021**, *104*, L201112.
(40) Kresse, G.; Furthmüller, J. Efficient iterative schemes for ab initio total-energy calculations using a plane-wave basis set. *Phys. Rev. B* **1996**, *54*, 11169.
(41) Blöchl, P. E. Projector augmented-wave method. *Phys. Rev. B* **1994**, *50*, 17953.
(42) Kresse, G.; Joubert, D. From ultrasoft pseudopotentials to the projector augmented-wave method. *Phys. Rev. B* **1999**, *59*, 1758.
(43) Perdew, J. P.; Burke, K.; Ernzerhof, M. Generalized gradient approximation made simple. *Phys. Rev. Lett.* **1996**, *77*, 3865.
(44) Perdew, J.; Burke, K.; Ernzerhof, M. Perdew, burke, and ernzerhof reply. *Phys. Rev. Lett.* **1998**, *80*, 891.
(45) Hedin, L. New method for calculating the one-particle Green's function with application to the electron-gas problem. *Phys. Rev.* **1965**, *139*, A796.
(46) Hybertsen, M. S.; Louie, S. G. First-principles theory of quasiparticles: calculation of band gaps in semiconductors and insulators. *Phys. Rev. Lett.* **1985**, *55*, 1418.
(47) Monkhorst, H. J.; Pack, J. D. Special points for Brillouin-zone integrations. *Phys. Rev. B* **1976**, *13*, 5188.
(48) Tkatchenko, A.; DiStasio, R. A., Jr; Car, R.; Scheffler, M. Accurate and efficient method for many-body van der Waals interactions. *Phys. Rev. Lett.* **2012**, *108*, 236402.
(49) Togo, A.; Tanaka, I. First principles phonon calculations in materials science. *Scr. Mater.* **2015**, *108*, 1−5.
(50) King-Smith, R. D.; Vanderbilt, D. Theory of polarization of crystalline solids. *Phys. Rev. B* **1993**, *47*, 1651−1654.
(51) Albrecht, S.; Reining, L.; Del Sole, R.; Onida, G. Ab initio calculation of excitonic effects in the optical spectra of semiconductors. *Phys. Rev. Lett.* **1998**, *80*, 4510.
(52) Sheoran, S.; Bhumla, P.; Bhattacharya, S. Emergence of cubic ordered full-plane persistent spin textures in lead-free materials. *Phys. Rev. Mater.* **2022**, *6*, 094602.
(53) Jin, K.-H.; Oh, E.; Stania, R.; Liu, F.; Yeom, H. W. Enhanced Berry Curvature Dipole and Persistent Spin Texture in the Bi(110) Monolayer. *Nano Lett.* **2021**, *21*, 9468−9475.
(54) Jia, F.; Hu, S.; Xu, S.; Gao, H.; Zhao, G.; Barone, P.; Stroppa, A.; Ren, W. Persistent spin-texture and ferroelectric polarization in 2D hybrid perovskite benzylammonium lead-halide. *J. Phys. Chem. Lett.* **2020**, *11*, 5177−5183.
(55) Bhumla, P.; Gill, D.; Sheoran, S.; Bhattacharya, S. Origin of Rashba Spin Splitting and Strain Tunability in Ferroelectric Bulk $CsPbF_3$. *J. Phys. Chem. Lett.* **2021**, *12*, 9539−9546.

https://doi.org/10.1021/acs.jpclett.2c03108
J. Phys. Chem. Lett. 2023, 14, 1494−1503

(56) Sheoran, S.; Kumar, M.; Bhumla, P.; Bhattacharya, S. Rashba spin splitting and anomalous spin textures in the bulk ferroelectric oxide perovskite KIO_3. *Mater. Adv.* **2022**, *3*, 4170−4178.
(57) Bernevig, B. A.; Orenstein, J.; Zhang, S.-C. Exact SU(2) symmetry and persistent spin helix in a spin-orbit coupled system. *Phys. Rev. Lett.* **2006**, *97*, 236601.
(58) Hu, T.; Jia, F.; Zhao, G.; Wu, J.; Stroppa, A.; Ren, W. Intrinsic and anisotropic Rashba spin splitting in Janus transition-metal dichalcogenide monolayers. *Phys. Rev. B* **2018**, *97*, 235404.
(59) Ai, H.; Ma, X.; Shao, X.; Li, W.; Zhao, M. Reversible out-of-plane spin texture in a two-dimensional ferroelectric material for persistent spin helix. *Phys. Rev. Mater.* **2019**, *3*, 054407.
(60) Absor, M. A. U.; Santoso, I.; Abraha, K.; Ishii, F.; Saito, M. Defect-induced large spin-orbit splitting in monolayer $PtSe_2$. *Phys. Rev. B* **2017**, *96*, 115128.
(61) Li, X.; Zhang, S.; Huang, H.; Hu, L.; Liu, F.; Wang, Q. Unidirectional spin−orbit interaction induced by the line defect in monolayer transition metal dichalcogenides for high-performance devices. *Nano Lett.* **2019**, *19*, 6005−6012.
(62) Cheng, C.; Sun, J.-T.; Chen, X.-R.; Fu, H.-X.; Meng, S. Nonlinear Rashba spin splitting in transition metal dichalcogenide monolayers. *Nanoscale* **2016**, *8*, 17854−17860.
(63) Jiang, J.; Li, R.; Mi, W. Electrical control of topological spin textures in two-dimensional multiferroics. *Nanoscale* **2021**, *13*, 20609−20614.
(64) Liu, C.; Gao, H.; Li, Y.; Wang, K.; Burton, L. A.; Ren, W. Manipulation of the Rashba effect in layered tellurides MTe (M= Ge, Sn, Pb). *J. Mater. Chem. C* **2020**, *8*, 5143−5149.
(65) Zhang, X.; Liu, Q.; Luo, J.-W.; Freeman, A. J.; Zunger, A. Hidden spin polarization in inversion-symmetric bulk crystals. *Nat. Phys.* **2014**, *10*, 387−393.
(66) Liu, Q.; Zhang, X.; Jin, H.; Lam, K.; Im, J.; Freeman, A. J.; Zunger, A. Search and design of nonmagnetic centrosymmetric layered crystals with large local spin polarization. *Phys. Rev. B* **2015**, *91*, 235204.
(67) Riley, J. M.; Mazzola, F.; Dendzik, M.; Michiardi, M.; Takayama, T.; Bawden, L.; Granerød, C.; Leandersson, M.; Balasubramanian, T.; Hoesch, M.; Kim, T. K.; Takagi, H.; Meevasana, W.; Hofmann, P.; Bahramy, M. S.; Wells, J. W.; King, P. D. C. Direct observation of spin-polarized bulk bands in an inversion-symmetric semiconductor. *Nat. Phys.* **2014**, *10*, 835−839.
(68) Yao, W.; Wang, E.; Huang, H.; Deng, K.; Yan, M.; Zhang, K.; Miyamoto, K.; Okuda, T.; Li, L.; Wang, Y.; Gao, H.; Liu, C.; Duan, W.; Zhou, S. Direct observation of spin-layer locking by local Rashba effect in monolayer semiconducting $PtSe_2$ film. *Nat. Commun.* **2017**, *8*, 1−6.
(69) Wu, S.-L.; Sumida, K.; Miyamoto, K.; Taguchi, K.; Yoshikawa, T.; Kimura, A.; Ueda, Y.; Arita, M.; Nagao, M.; Watauchi, S.; Tanaka, I.; Okuda, T. Direct evidence of hidden local spin polarization in a centrosymmetric superconductor $LaO_{0.55}F_{0.45}BiS_2$. *Nat. Commun.* **2017**, *8*, 1−7.
(70) Yuan, L.; Liu, Q.; Zhang, X.; Luo, J.-W.; Li, S.-S.; Zunger, A. Uncovering and tailoring hidden Rashba spin-orbit splitting in centrosymmetric crystals. *Nat. Commun.* **2019**, *10*, 1−8.

https://doi.org/10.1021/acs.jpclett.2c03108
J. Phys. Chem. Lett. 2023, 14, 1494−1503